

Article

Study on the Evolution of Physicochemical Properties of Carbon Black at Different Regeneration Stages of Diesel Particulate Filters Regenerated by Non-Thermal Plasma

Yong Luo, Yunxi Shi , Kaiqi Zhuang, Ruirui Ji, Xulong Chen, Yankang Huang, Zhe Wang, Yixi Cai and Xiaohua Li

School of Automotive and Traffic Engineering, Jiangsu University, Zhenjiang 212013, China; eternity0210@163.com (Y.L.); zhuangkaiqi2004@126.com (K.Z.); jrrujs@126.com (R.J.); chenxulong307@163.com (X.C.); hyk2930592802@163.com (Y.H.); wz163162024@163.com (Z.W.); qc001@ujs.edu.cn (Y.C.); lixiaohua@ujs.edu.cn (X.L.)

* Correspondence: shiyunxi880527@126.com

Abstract: As a new type of aftertreatment technology, non-thermal plasma (NTP) can effectively decompose the particulate matter (PM) deposited in diesel particulate filters (DPFs). In this paper, a regeneration test of a DPF loaded with carbon black was carried out using an NTP injection system, and the changes of oxidative activity, elemental content, and occurrence state, microstructure and graphitization degree of carbon black were analyzed to reveal the evolution of the physicochemical properties of carbon black at different regeneration stages of the DPF regenerated by NTP. As the regeneration stage of the DPF advanced, T_i , T_{max} , and T_e of the carbon black at the bottom of the DPF decreased, which were higher than those at the regeneration interface. After the NTP reaction, the proportion of C element decreased to less than 80%, while the proportion of O element increased to more than 20%; C-O was converted to C=O and the relative content of C=O increased. The average microcrystalline length and average spacing decreased, while the average microcrystalline curvature increased. The I_{D1}/I_G (relative peak intensities) of carbon black samples decreased from 3.31 to 3.10, and the $R3$ (relative peak intensities, $R3 = I_{D3}/(I_G + I_{D2} + I_{D3})$) increased from 0.41 to 0.58. The content of carbon clusters had a great influence on the disorder of the microcrystalline structure, so the graphitization degree of carbon black decreased and the oxidation activity increased.

Keywords: diesel particulate filter; regeneration; non-thermal plasma; carbon black; oxidation



Citation: Luo, Y.; Shi, Y.; Zhuang, K.; Ji, R.; Chen, X.; Huang, Y.; Wang, Z.; Cai, Y.; Li, X. Study on the Evolution of Physicochemical Properties of Carbon Black at Different Regeneration Stages of Diesel Particulate Filters Regenerated by Non-Thermal Plasma. *Processes* **2024**, *12*, 1113. <https://doi.org/10.3390/pr12061113>

Academic Editor: Jiaqiang E

Received: 30 March 2024

Revised: 8 May 2024

Accepted: 22 May 2024

Published: 28 May 2024



Copyright: © 2024 by the authors. Licensee MDPI, Basel, Switzerland. This article is an open access article distributed under the terms and conditions of the Creative Commons Attribution (CC BY) license (<https://creativecommons.org/licenses/by/4.0/>).

1. Introduction

Diesel engines have the advantages of high torque, good economic performance, low speed, and high safety, and are widely used in industrial fields such as construction machinery, large cargo transportation, and electric power [1,2]. However, particulate matter (PM) emitted from diesel engines can cause serious harm to the environment and human health [3]. PM can cause a variety of health problems such as eye irritation, nasal allergy, coughing, and breathing difficulties in humans. Prolonged exposure to PM may also lead to serious respiratory diseases and heart diseases [4]. Diesel particulate filters (DPFs) can effectively capture PM and prevent it from entering the atmosphere, and are currently the most effective solution [5]. However, over time, a DPF's channels will be blocked by PM and the exhaust back pressure increases. When the back pressure of the diesel engine exceeds a certain limit, its working performance decreases significantly and the DPF needs to be regenerated [6].

The strong oxidizing substances in a non-thermal plasma (NTP) have been shown to be effective in decomposing PM in diesel engines [7,8]. Ma et al. [9] introduced exhaust gas with PM into an NTP generator for reaction. It was shown that the total number and mass of PM were reduced by 40% and 76.9%, respectively. And the purification rate of PAHs in the particulate phase was 58.4% after NTP treatment. Liu et al. [10] conducted

removal tests of PM at lower temperature conditions via synergistic action of NTP and $\text{MnO}_x/\text{CeO}_2$ catalysts. It was shown that the removal efficiencies of PM reached 85.2% and 94.3% at 20 °C and 200 °C, respectively. Fushimi et al. [11] carried out experiments on the oxidative decomposition of PM in a dielectric barrier NTP reactor with different structures, and pointed out that O_3 and NO_2 were the main active substances for the oxidation of PM, and the decomposition products of PM were CO and CO_2 . Based on this research, scholars have applied NTP technology to the field of DPF regeneration. Hongsuk et al. [12] tested regeneration of a DOC + DPF system by entering compressed air into the generator in a rotating manner to produce rotating NTP. It was shown that the rotating plasma generator had good durability under vehicle driving conditions, and the regeneration efficiency of a DPF containing 5.5 g/L carbon was 93%. Shi et al. [13–15] investigated the effect of initial regeneration temperature on a DPF regenerated by NTP, and found that the higher the temperature the lower the amount of PM decomposition, and that the peak temperature and temperature gradient inside the DPF were much lower than the failure limit value. The effect of ambient temperature on the regeneration performance of DPFs has been investigated, and NTP can effectively regenerate a DPF without a catalyst, demonstrating superiority compared to the conventional regeneration.

Carbon black, as a cheap and readily available material with similar physicochemical properties to PM, is gradually replacing diesel PM for DPF regeneration studies [16–18]. Naseri et al. [19] used a thermal gravimetric analyzer (TGA) and high resolution transmission electron microscope (HRTEM) to characterize carbon black samples untreated, and heat-treated to 1400 °C and 1600 °C. The oxidation of carbon black was found to follow the steps of surface oxidation, nanochannel formation, and microcrystalline oxidation. Tighe et al. [20] performed oxidation tests on diesel PM and carbon black at the temperature range of 450 °C to 550 °C. It was found that the internal channel structures of the spherical particles of both were consistent. During the combustion process, the channels of the primary carbon particles of both were gradually enlarged, while O_2 entered the interior of the particles to oxidize the carbon microcrystals. Meng et al. [21,22] conducted thermogravimetric analysis of carbon black and regeneration test studies on a DPF loaded with carbon black. The study showed that the oxidation process of carbon black went through the process of organic matter volatilization, amorphous carbon oxidation, graphitization, and combustion of carbon black particles, and the gas emission was mainly concentrated in the rapid regeneration period of the DPF. Fang et al. [23] loaded a mixture of carbon black and different masses of ash into the DPF for the regeneration test. It was shown that a larger ash loading was conducive to improving the regeneration efficiency of the DPF, and the regeneration efficiency increased by 47% when the ash loading was increased from 0 g/L to 10 g/L. Chen et al. [24] constructed an experimental system to regenerate a DPF loaded with carbon black by oxidizing NTP, and investigated the influence of NTP injection flow rate on the removal rate of carbon black and the regeneration of the DPF. It was shown that the DPF regeneration efficiency increased and then decreased with the increase of NTP injection flow rate. The highest DPF regeneration efficiency of 85.1% was achieved when the NTP injection flow rate was 30 L/min. Most previous research mainly focuses on improving the regeneration efficiency of DPFs. However, few research studies focus on the decomposition mechanism and evolution of carbon black during the DPF regeneration process.

In this study, a DPF loaded with carbon black was regenerated using an NTP generator and the carbon black was sampled at different stages of regeneration. The oxidation characteristics, elemental ratio and occurrence state, micro-structure, and graphitization degree of the carbon black were analyzed using TGA, X-ray photoelectron spectroscopy (XPS), HRTEM, and Raman spectra (RNS) to study the changes in physical and chemical properties of carbon black during the regeneration process of the DPF. The changes in physical and chemical properties were investigated to provide a theoretical basis and experimental basis for the evolution of carbon black by NTP oxidative decomposition.

2. Experimental System and Research Methodology

2.1. DPF Loaded Carbon Black Test System

Figure 1 illustrates the schematic diagram of the DPF loading carbon black device, which mainly includes filters, air compressor, vacuum pump, a DPF, and piping. The DPF (NGK Environmental Ceramics Co., Suzhou, China) used in the test is made of cordierite ceramic, and its structural parameters are shown in Table 1. The carbon black (Orion Inc., Espoo, Finland) is Printex-U, and its parameters are shown in Table 2.

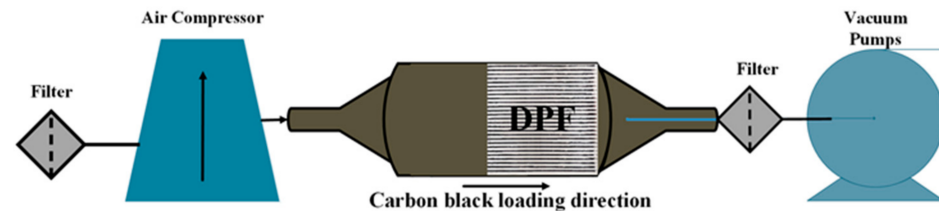


Figure 1. Schematic diagram of the device for loading carbon black into DPF. Reproduced with permission from Xulong Chen, Yunxi Shi et al., Carbon Letters; published by MDPI, 2023 [24].

Table 1. DPF structural parameters. Reproduced with permission from Xulong Chen, Yunxi Shi et al., Carbon Letters; published by MDPI, 2023 [24].

DPF	Parameter
Diameter × length/mm	144 × 152
Wall thickness/mm	0.46
Number of holes/cpsi	100
Volume/L	2.48
Material	cordierite
Maximum operating temperature/°C	1200

Table 2. Physical properties of carbon black. Reproduced with permission from Xulong Chen, Yunxi Shi et al., Carbon Letters; published by MDPI, 2023 [24].

Printex-U	Parameter
Particle size/nm	25
Ash/%	0.02
Volatile matter (950 °C)/%	5
BET/m ² ·g ^{−1}	92

2.2. NTP-Regenerative DPF Test System

Figure 2 illustrates the schematic diagram of the experimental NTP-regenerated DPF system, which includes an NTP generator injection system and a DPF regeneration system. The NTP generator had a coaxial cylindrical structure of dielectric barrier discharge type, the barrier dielectric layer was comprised of a quartz glass tube, and the stainless steel tube and the steel mesh were used as the low-pressure electrode and high-pressure electrode, respectively. The generator utilized a combination of internal water cooling and external air cooling, with an infrared thermometer monitoring the surface temperature in the NTP generator discharge region. The NTP generator was powered by a CTP-2000K intelligent electronic shock machine. The TDS3034B digital oscilloscope monitored the working voltage and frequency of the NTP generator. A voltage divider capacitor was used in the circuit to assist in the measurement of the discharge voltage, and the capacitance ratio of the voltage divider capacitor was $C_1:C_2 = 1:1000$. An oxygen generator controlled the flow of oxygen injected into the NTP reactor. Oxygen was ionized by the NTP generator and converted into strong oxidizing reactive particles (O_3 , O , etc.). The DPF regeneration system consisted of a DPF regeneration device alongside testing and analysis instruments. A gas analyzer was used to monitor the volume fraction of CO_x , the decomposition product

of carbon black decomposition product at the back end of the DPF. An O_3 analyzer was used to monitor the mass concentration of O_3 at the inlet and outlet ends of the DPF. The temperature inspector monitored the internal temperature of the DPF. Figure 3 illustrates the distribution of thermocouples inside the DPF.

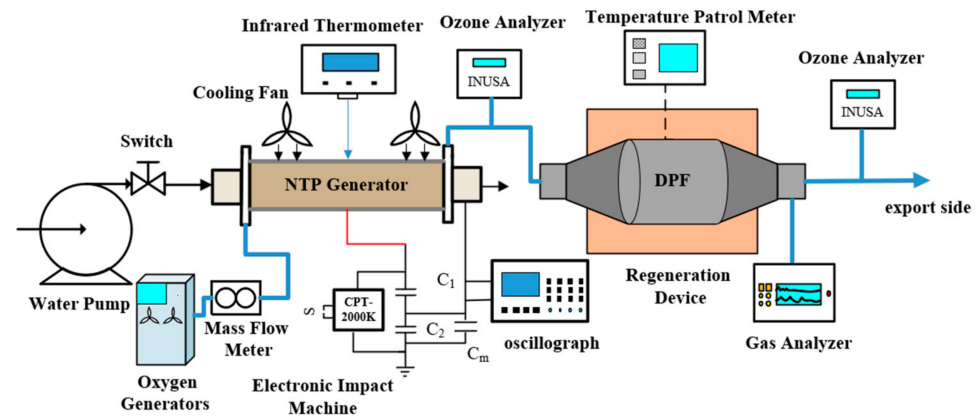


Figure 2. Schematic diagram of NTP-regenerated DPF test system. Reproduced with permission from Xulong Chen, Yunxi Shi et al., Carbon Letters; published by MDPI, 2023 [24].

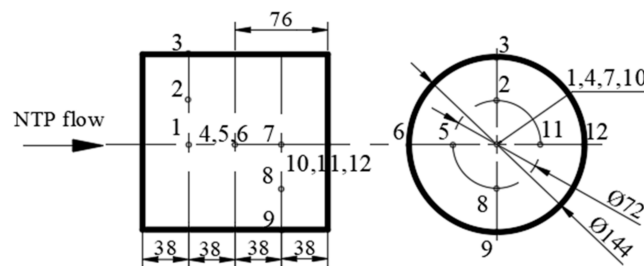


Figure 3. Schematic distribution of thermocouple positions inside the DPF. Reproduced with permission from Xulong Chen, Yunxi Shi et al., Carbon Letters; published by MDPI, 2023 [24].

2.3. DPF Regeneration Test Method

The oxidative decomposition of carbon black is exothermic, and the temperature of each measurement point inside the DPF illustrates a tendency of increasing and then decreasing with the regeneration of the DPF. When the temperature at the measurement point decreases, it can be assumed that the carbon black in the channel of the DPF has been completely oxidized and decomposed by the NTP active substance [25]. The flow rate of NTP was 30 L/min, and the initial regeneration temperature was 20 °C, and the initial loading of carbon black was 6 g/L. The DPFs were reacted separately at different regeneration stage, and the DPFs were dissected along the median axis, as shown in Figure 4. The carbon black samples were taken from the regeneration interfaces and the bottom of the DPF. Figure 4a illustrates the profile of DPF1, regenerated to 1/4; Figure 4b illustrates the profile of DPF2 regenerated to 1/2; Figure 4c illustrates the profile of DPF3 regenerated to 3/4; Figure 4d illustrates the profile of DPF4, which was basically regenerated completely and the retained portion was used for sampling. The red and orange boxes in Figure 4 are the carbon black sampling positions of the DPF regeneration interface and the bottom, identified by 1~6. The regeneration interfaces of DPF3 and DPF4 were close to the bottom, so the samples were taken from the same position. Table 3 illustrates the maximum temperature of regeneration at the carbon black sampling position, and sample 0 is the initial carbon black before the DPF regeneration. The maximum temperature at the sampling position at the bottom of the DPF increased as the regeneration stage of the DPF advanced, and the maximum temperature of the sampling position at the regeneration interface of the DPF was higher than that of the bottom at the same regeneration stage.

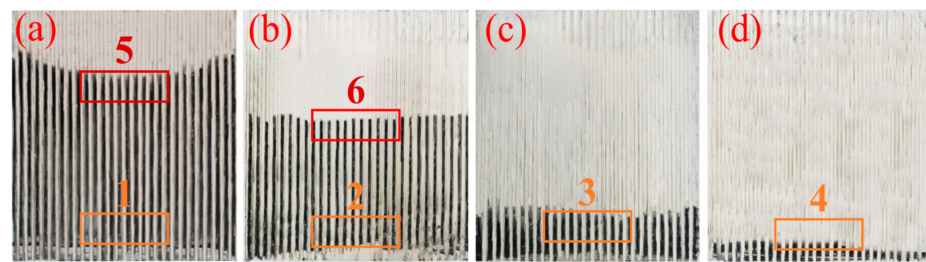


Figure 4. Axial section of DPF after regeneration: (a) DPF1, (b) DPF2, (c) DPF3, (d) DPF4.

Table 3. Maximum temperatures of temperature measurement points at the regeneration of carbon black samples.

Sample Name	Temperature Measurement Point Number	Temperature/°C
0 (Original machine carbon black)	\	\
1 (DPF1 bottom)	10	148.7
2 (DPF2 bottom)	10	183.0
3 (DPF3 bottom)	10	231.1
4 (DPF4 bottom)	10	239.3
5 (DPF1 interface)	1	241.3
6 (DPF2 interface)	4	272.8

The thermogravimetric properties of the carbon black samples were analyzed using a TGA8000 thermogravimetric analyzer, and the thermogravimetric test procedure is shown in Table 4. The program setting of N₂ atmosphere ensures the complete volatilization of the volatile fraction (VF) and the effective separation of the VF from the elemental carbon (EC) [26]. EscaLab 250Xi XPS (Thermo Fisher Scientific, Waltham, MA, USA) was used to determine and analyze the elemental species, relative content, and the fugitive states of the carbon black samples [27]. The morphology and structure of primary carbon particles of the carbon black samples were measured using a JEOL-2100 F transmission electron microscope (Thermo Fisher Scientific, Waltham, MA, USA). The magnifications of carbon black samples were 50,000 and 2 million times, respectively. The degree of graphitization of the carbon black samples was analyzed using a DXR-type laser Raman spectrometer (Thermo Fisher Scientific, Waltham, MA, USA). The testing process was performed for 30 consecutive scans with a spectral scanning range of 50 cm^{−1} to 3400 cm^{−1}. Different regions of the same sample were tested to ensure the accuracy of the results of the test samples [28].

Table 4. Thermogravimetric test procedure. Reproduced with permission from Xulong Chen, Yunxi Shi et al., Carbon Letters; published by MDPI, 2023 [24].

Step	Program Temperature	Atmosphere and Flow
1	50 °C for 1 min	Nitrogen 60 mL/min
2	Temperature increase to 450 °C at a rate of 10 °C/min	Nitrogen 60 mL/min
3	450 °C for 1 min	Nitrogen 60 mL/min
4	Cool down to 50 °C at a rate of 10 °C/min	Nitrogen 60 mL/min
5	50 °C for 1 min	Oxygen 20 mL/min + Nitrogen 40 mL/min
6	Increase the temperature to 750 °C at a rate of 10 °C/min.	Oxygen 20 mL/min + Nitrogen 40 mL/min
7	750 °C for 1 min	Oxygen 20 mL/min + Nitrogen 40 mL/min

3. Test Results and Analysis

3.1. Oxidation Characteristics of Carbon Black Samples

Figure 5 illustrates the TG and DTG curves of the carbon black samples. The carbon black samples have less VF content, and three specific temperatures in the EC oxidation process can be chosen as the characteristic parameters for evaluating the oxidizing activity of the carbon black: 1. the ignition temperature T_i (the temperature corresponding to the initial mass loss of 10% during the oxidation reaction); 2. the maximum oxygen oxidation

rate temperature T_{max} (the temperature corresponding to the maximum mass loss rate is the lowest point of the DTG curve.); 3. the final combustion temperature T_e (the temperature appearing in a mass loss of 90%).

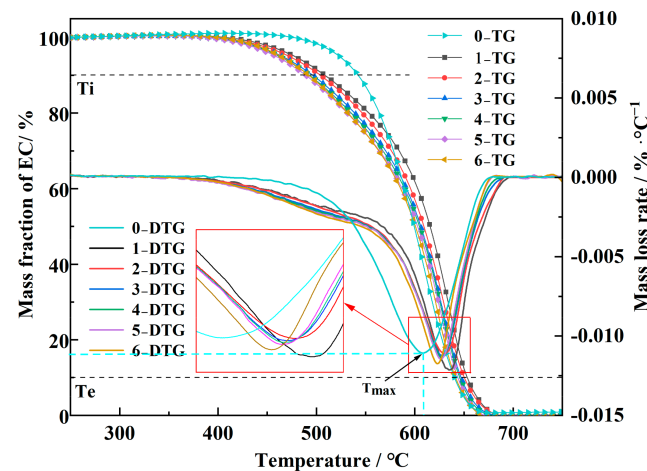


Figure 5. TG and DTG curves of carbon black samples.

The T_i , T_{max} , and T_e of carbon black sample 0 were 543.6 °C, 604.5 °C, and 640.3 °C, respectively. After the NTP reaction, T_i of the carbon black sample decreased and the T_{max} and T_e increased. As the DPF regeneration stage advances, the T_i , T_{max} , and T_e of carbon black samples 1~4 at the bottom position are decreasing. The T_i of carbon black samples 1~4 decreased from 513.5 °C to 492.8 °C, T_{max} from 636.3 °C to 627.7 °C, and T_e from 652.4 °C to 641.4 °C. The T_i , T_{max} , and T_e at the regeneration interface in the same regeneration stage of the DPF were less than those at the bottom sampling position. The lower the apparent activation energy of the carbon black samples, the easier the oxidation reaction occurs and the higher its oxidation activity. The apparent activation energy of carbon black was calculated by the Arrhenius equation [29,30], as shown in Equation (1).

$$\ln \left[-\frac{dm}{m_0 dt} \right] = \ln [A \cdot P_{O_2}] - \frac{E_a}{RT} \quad (1)$$

where m_0 is the initial mass of the sample, mg; t is the length of time the sample is oxidized, s; A is the finger forward factor, s^{-1} ; P_{O_2} is the partial pressure of O_2 in the heated atmosphere, Pa; E_a is the apparent activation energy, kJ/mol; R is the molar gas constant, 8.314 J/mol·K; and T is the oxidation temperature, K.

The activation energy of carbon black sample 0 before DPF regeneration was 179.89 kJ/mol. The activation energy of carbon black samples 1~4 at the bottom sampling position decreased from 156.5 kJ/mol to 125.7 kJ/mol, and the activation energies of carbon black samples 5 and 6 at the regeneration interface were 117.91 kJ/mol and 109.62 kJ/mol as the regeneration stage of the DPF advanced. The activation energy of sample 0 before DPF regeneration was the highest, and a higher ignition temperature was needed to achieve rapid oxidation of carbon black. The activation energies of carbon black samples 1~6 were all reduced after the NTP reaction. The activation energy of carbon black samples 1~4 at the bottom position of the DPF decreased continuously and the oxidation activity increased as the regeneration stage advanced. The activation energy of carbon black samples 5~6 at the regeneration interface was lower than those at the bottom sampling position. The NTP active substance was easy to decompose by heat, and in addition, the concentration of NTP active substances gradually decreased as they react with carbon black during the process of passing from the top to the bottom of the DPF. Under the combined effect of high NTP active substance and the reaction temperature, the oxidative decomposition of the regeneration interface between NTP and carbon black was more intense compared with that of the bottom, and so was the oxidation activity of carbon black. The oxidative

decomposition reaction between NTP and carbon black at the regeneration interface was more intense than that at the bottom, and the oxidation process of carbon black was faster.

3.2. Elemental Content and State of Carbon Black Samples

Each carbon black sample was fully dried and the sample powder was ground, and then the sample was spread on double-sided adhesive and placed at the center of clean aluminum foil (wiped with acetone). Another piece of aluminum foil covering the sample was placed on the platform of the tableting machine to pull the pressure bar to 10 MPa, and the sample to be tested was made into a 1 cm × 1 cm tablet for a period of time. In the XPS narrow scan analysis, the carbon C1s with a binding energy of 284.6 eV was used to correct the measurement results by deducting the charge effect and performing multi-peak fitting.

Figure 6 illustrates the full spectrum of the XPS scan of the carbon black samples. The C and O elements in the carbon black samples were scanned narrowly, and the peaks were fitted using Origin2021 software (OriginLab Corp., Northampton, MA, USA). The occurrence state and content of C and O elements were analyzed according to the area of photoelectron peaks in the energy spectrum [31]. The significant elemental peaks were observed near 248 eV and 532 eV, corresponding to C1s and O1s spectra. The scanned full spectrum of each carbon black sample can be used to calculate its relative content ratios of C and O elements, as shown in Table 5. The relative contents of C and O in sample 0 were 88.4% and 11.6% before regeneration. The relative content of C element in carbon black decreased to below 80% and the content of O element increased to more than 20% after the NTP reaction. As the reaction proceeded, the relative content of O element in carbon black samples 1~4 gradually increased from 20.9% to 22.8%. The relative content of O element at the regeneration interface at the same stage was higher than that at the bottom. The elevation of the relative content of elemental O in the samples indicates that part of C element combined with O element and existed in the carbon black in an incompletely oxidized state, so the oxidizing activity of carbon black was elevated [32], which was consistent with the analytical results of TG.

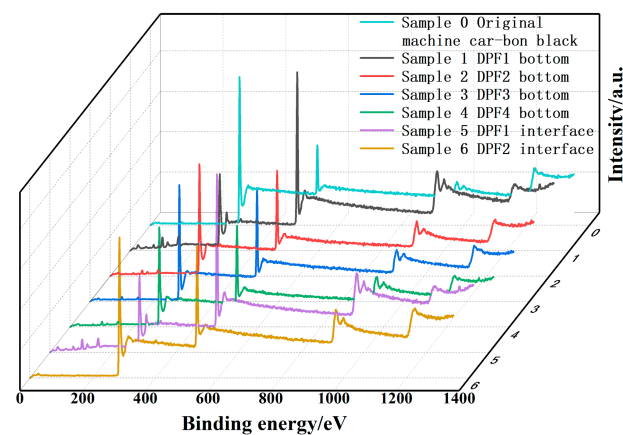


Figure 6. Full spectrum of XPS scan of carbon black samples.

Table 5. Relative content of major elements in carbon black samples at different regeneration stages of DPF.

Sample Name	C/%	O/%
0	88.4	11.6
1	79.1	20.9
2	78.5	21.5
3	77.8	22.2
4	77.3	22.8
5	71.9	28.1
6	71.9	28.1

In order to analyze the oxidation state of carbon black more intuitively, the C and O elements of each sample were narrowly scanned and split-peak fitted to analyze the state of elemental assignment and its relative content. Figure 7 illustrates an example of the peak-fitting curve of the C1s elemental spectrum. The common assignment patterns of C elements are as follows: carbon–carbon and carbon–hydrogen bonds (C-C, C=C, C-H) in hydrocarbons, corresponding to electron binding energy peaks of 284.6 eV~285.0 eV; carbon–oxygen single bonds (C-O, C-O-H) in ethers and hydroxyls, corresponding to electron binding energy peaks of 285.3 eV~286.8 eV; carbon–oxygen double bonds in carbonyls (C=O), carboxyl carbon (O-C=O), corresponding to the peak electron binding energy of 286.3 eV~287.8 eV.

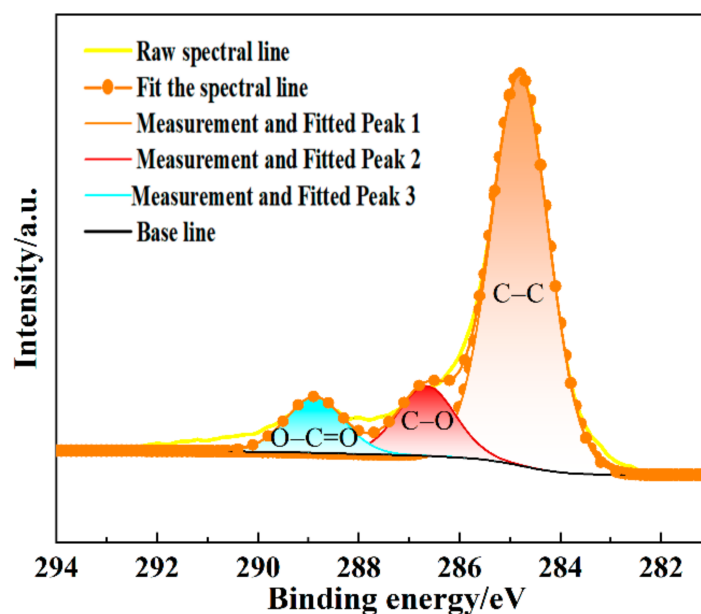


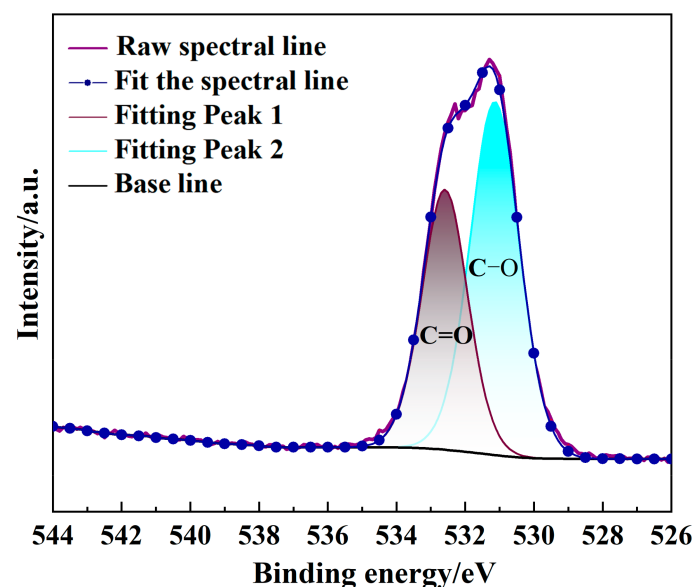
Figure 7. Example of fitted curves for C1s elemental spectra. Reproduced with permission from Xulong Chen, Yunxi Shi et al., Carbon Letters; published by MDPI, 2023 [24].

Table 6 illustrates the relative content of C1s spectrum in the carbon black samples in different occurrence states. Most of the C atoms in carbon black were not bound to O atoms and this type of C atom in Sample 0 accounted for 77.2% of the total C atoms. In sample 0, there are C atoms bound to two O atoms, which accounted for 8.13% of the total C atoms. The C atoms content of samples 1–4 in the form of C-C and C atoms bound to two O atoms in the form of carboxyl groups and lipid bonds decreased and the content of C atoms bound to one O atom in the form of ethers, hydroxyl groups, and carbonyl groups increased by 3.56% after NTP oxidation reaction. The content of C atoms in the form of C-C at the regeneration interface was lower than at the bottom at the same stage. Due to the interaction of high-energy ions and free radicals in the NTP active substance, C atoms underwent oxidation reactions to produce oxygen-containing functional groups. These oxygen-containing functional groups could increase the oxidizing activity of carbon black and make it easier to react with NTP [33,34]. It was shown that after the reaction with NTP-reactive substances, C atoms bound with two O atoms were oxidized to CO₂, while some C-C bonds were oxidized to C-O bonds. The oxygen-containing functional groups of carbon black increased significantly, and the oxidative activity of carbon black was enhanced [35].

Table 6. Relative content of different fugacity states of C1s spectra in carbon black samples.

Sample Name	C-C/%	C-O/%	O-C=O/%
0	77.2	14.6	8.1
1	75.7	16.4	8.0
2	75.6	16.5	7.8
3	75.0	18.0	7.1
4	73.8	20.0	6.2
5	72.3	21.6	6.1
6	71.3	23.1	5.6

Figure 8 shows an example of the split-peak fitting curve of the O1s elemental spectrum. The O element existed in the form of carbon–oxygen single bond (C–O) and carbon–oxygen double bond (C=O), corresponding to the peak positions of the electronic binding energies of 531.0 eV~531.8 eV and 532.3 eV~533.0 eV, respectively [36]. Table 7 illustrates the relative contents of different occurrence states of O1s spectra in carbon black samples. After the NTP oxidation reaction, the content of O atoms in the form of C–O in carbon black samples 1~4 gradually decreased, and the content of O atoms in the form of C=O gradually increased. The content of C atoms in the form of C–O at the regeneration interface was lower than that at the bottom at the same stage. This phenomenon indicates that the oxygen-containing functional groups are mainly present in carbon black in the form of C–O. As the regeneration stage progresses, C–O was converted to C=O, and the relative content of C=O in the carbon black sample increased.

**Figure 8.** Example of fitted curves for O1s elemental spectra. Reproduced with permission from Xulong Chen, Yunxi Shi et al., Carbon Letters; published by MDPI, 2023 [24].**Table 7.** Relative content of different fugacity states of O1s spectra in carbon black samples.

Sample Name	C=O/%	C-O/%
0	62.7	37.3
1	60.7	39.3
2	59.4	40.6
3	59.4	40.6
4	58.7	41.3
5	55.2	44.8
6	53.1	47.0

3.3. Micro-Nano Structure of Carbon Black Samples

The carbon black samples at the regeneration interface and the bottom sampling position were immersed in anhydrous ethanol, and the suspension was prepared by centrifugal extraction for 20 min using an ultrasonic oscillator. A sampler was used to drop the suspension on a support membrane (copper material) for sufficient drying before shooting. The morphology and structure of primary carbon particles of the carbon black and PM samples were measured using JEOL-2100 F transmission electron microscopy.

Figure 9 illustrates the aggregated morphology and core-shell structure of primary carbon particles of the carbon black samples obtained from TEM. Carbon black consists of dozens to tens of spherical primary particles forming a chain or cluster flocculent structure, which is due to van der Waals force and electrostatic gravity between particles [37,38]. The stacking of primary carbon particles in carbon black samples 1 to 4 gradually decreased and evolved from a cluster floc structure to a chain structure as the DPF regeneration stage advanced. As the NTP regeneration of the DPF advanced, NTP active substance entered into the internal cluster flocculated structure of particles through free diffusion and forced convection. The weaker part of the cluster flocculated structure was the first one to break under the oxidizing effect of the NTP active substance, and the cluster flocculated structure decomposed into the chain-like structure [39]. The aggregated morphology of primary carbon particles of carbon black samples 5~6 showed a clear chain-like structure. The surface charge of some carbon particles increased after being oxidized by NTP, leading to an increase in the electrostatic attraction between the particles. And this interaction caused the carbon particles to be more tightly packed together, thus reducing the particle size of the aggregated state [40].

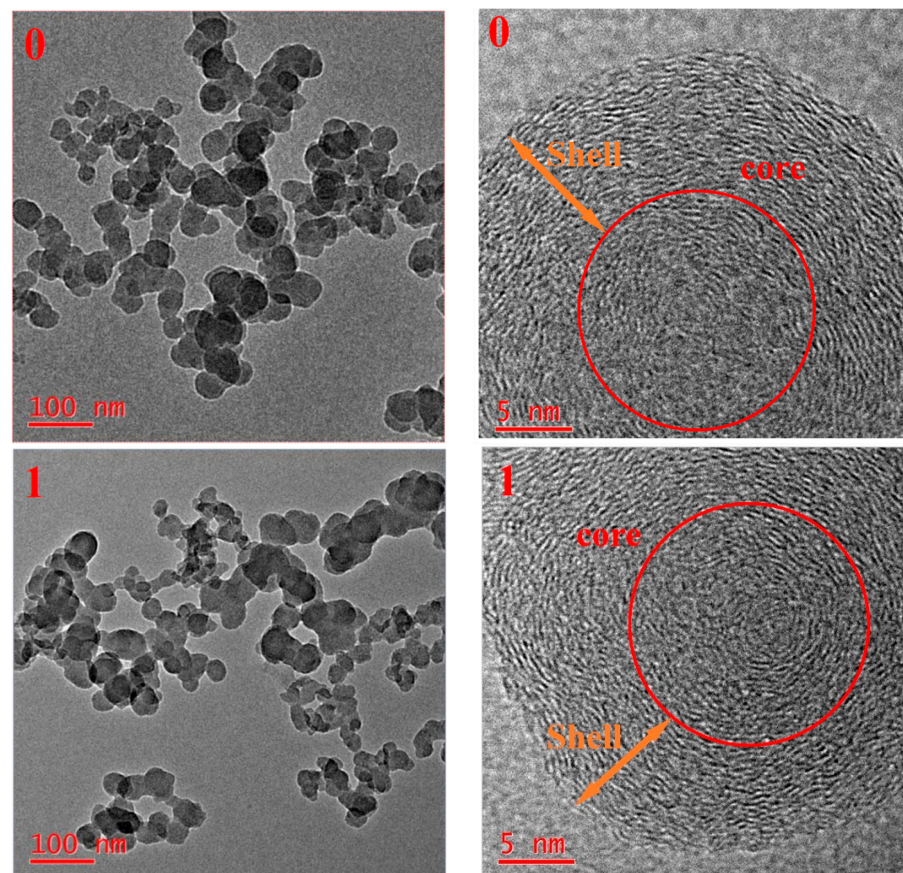


Figure 9. Cont.

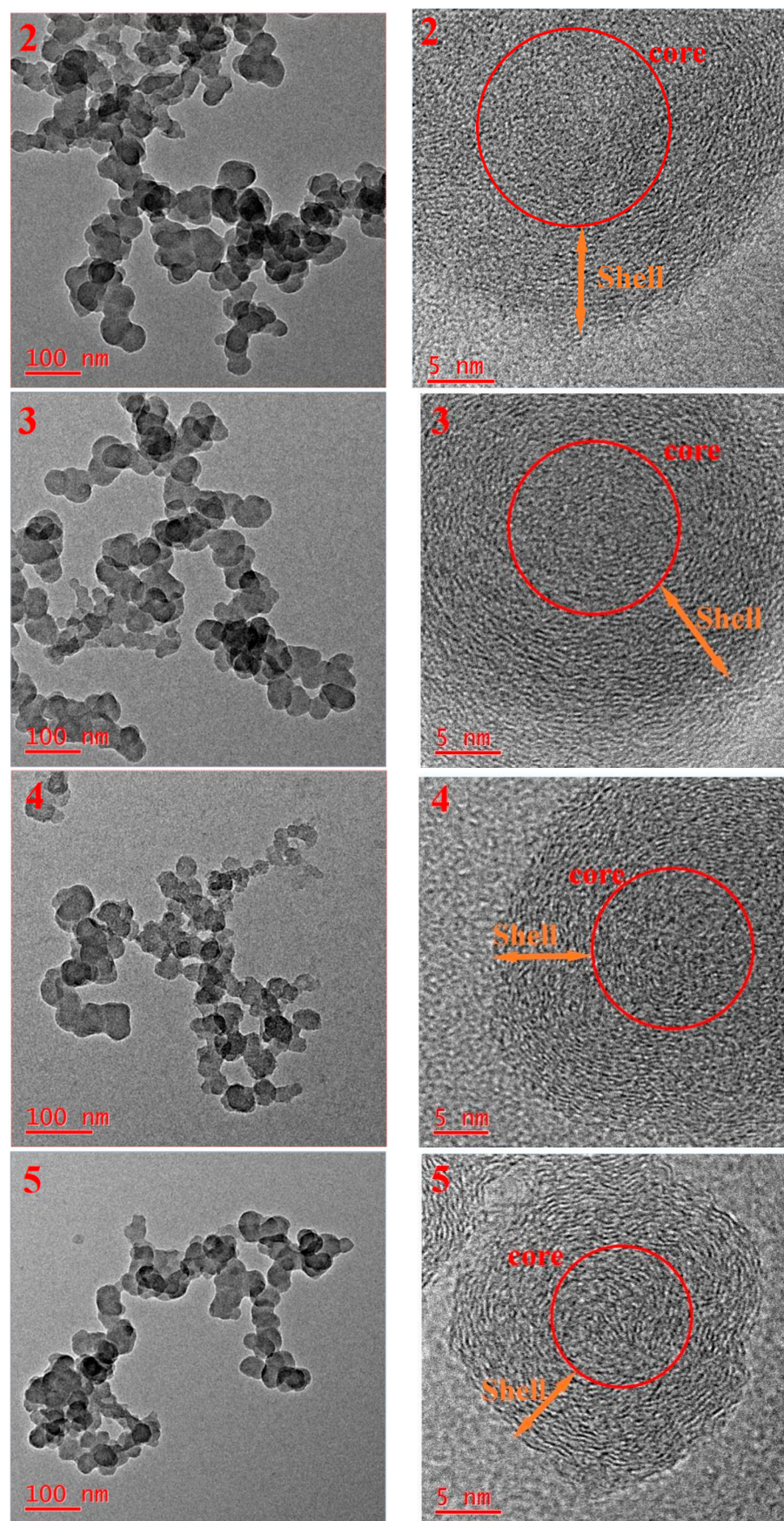


Figure 9. Cont.

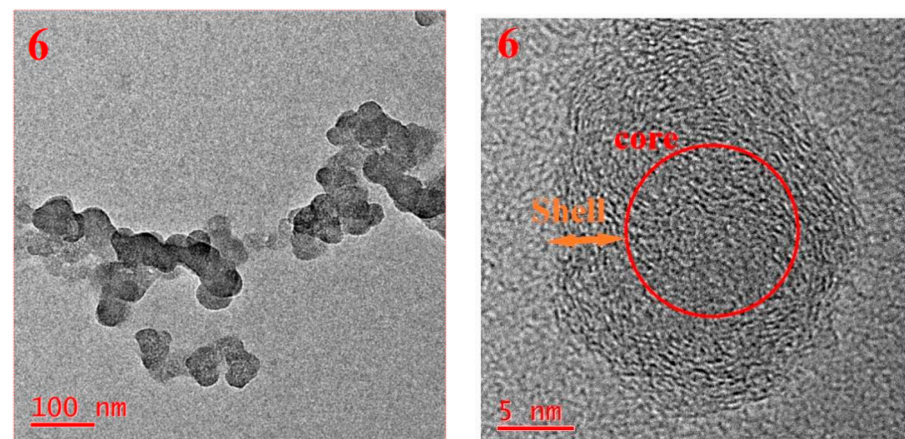


Figure 9. Aggregation pattern (left) and core-shell structure (right) of primary carbon particles of carbon black samples.

The primary carbon black particles are spherical core-shell structures with diameters of about 20 nm~35 nm, with the outer shell consisting of longer microcrystals stacked layer by layer to form a graphite layer-like structure, and the inner core consisting of disordered microcrystals stacked haphazardly with shorter lengths. The primary carbon particles in Sample 0 had more amorphous carbon components in the core, and the boundary of the outer shell was obvious and clearly distinguishable. The diameter of primary carbon particles in carbon black samples 1~4 decreased as the DPF regeneration stage advanced, and the diameter of primary carbon particles at the regeneration interface was smaller than that at the bottom at the same regeneration stage, and the boundary between the kernel and the shell was gradually blurred. The presence of unpaired sp_2 electrons at the edges of carbon microcrystals made it easier for them to combine with C atoms in the NTP actives, eroding the edges of the carbon particles, and the C is removed as CO or CO₂, while some of the long microcrystals were cleaved into short microcrystals [41,42]. Figure 10 shows the schematic diagram of extracting characteristic parameters of primary carbon particle microcrystals.

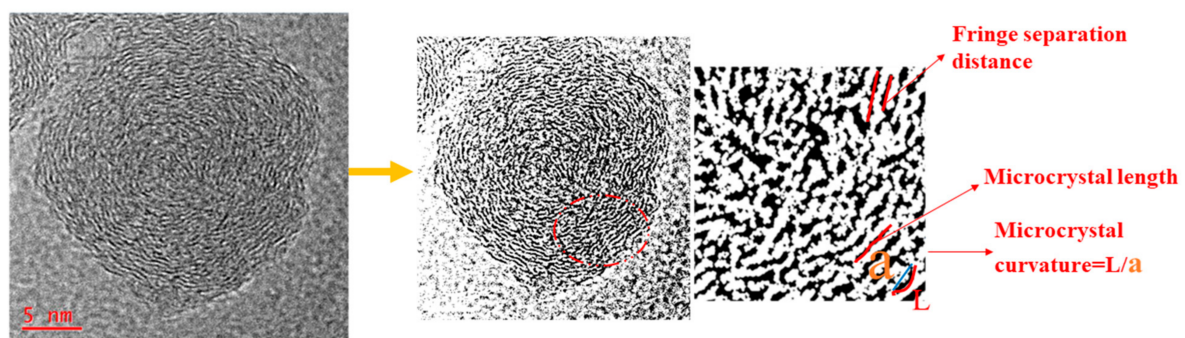


Figure 10. Schematic diagram of the extraction of the characteristic parameters of primary carbon particle microcrystals. Reproduced with permission from Yunxi Shi, Yinqin Yang et al., Fuel; published by Elsevier, 2024 [43].

Figure 11 illustrates the distribution of microcrystal length (L_a) in primary carbon particles in the carbon black samples. The average value of L_a in sample 0 was 0.48 nm, and 80% of the microcrystalline size was concentrated in the range of 0.19 nm~0.97 nm. The microcrystalline lengths of carbon black samples 1~4 gradually decreased and the average value of L_a in samples 1~4 after oxidation gradually decreased from 0.33 nm to 0.27 nm as the regeneration stage advanced. The range of microcrystal length distribution in the primary carbon particles also significantly reduced, with a significantly higher percentage of microcrystals with lengths ranging from 0.12 nm to 0.80 nm. The presence of unpaired sp_2 electrons at the microcrystalline edges of the primary carbon particles made it easier for

the carbon particle components to combine with the O atoms in the NTP active substances and be removed from the surface of the primary carbon particles in the form of CO or CO₂. NTP preferentially reacted with the physically defective parts of the longer microcrystals to form shorter microcrystals. Therefore, the average microcrystal length was significantly reduced after NTP treatment [43]. The microcrystal length at the regeneration interface at the same stage was smaller than that at the bottom, and the average values of La in samples 5 and 6 were 0.26 nm and 0.22 nm. The oxidative decomposition reaction between NTP and carbon black at the regeneration interface was more intense compared with that at the bottom, and more long microcrystals were cleaved to form shorter microcrystals, so that the length of the microcrystals was shorter than that at the bottom.

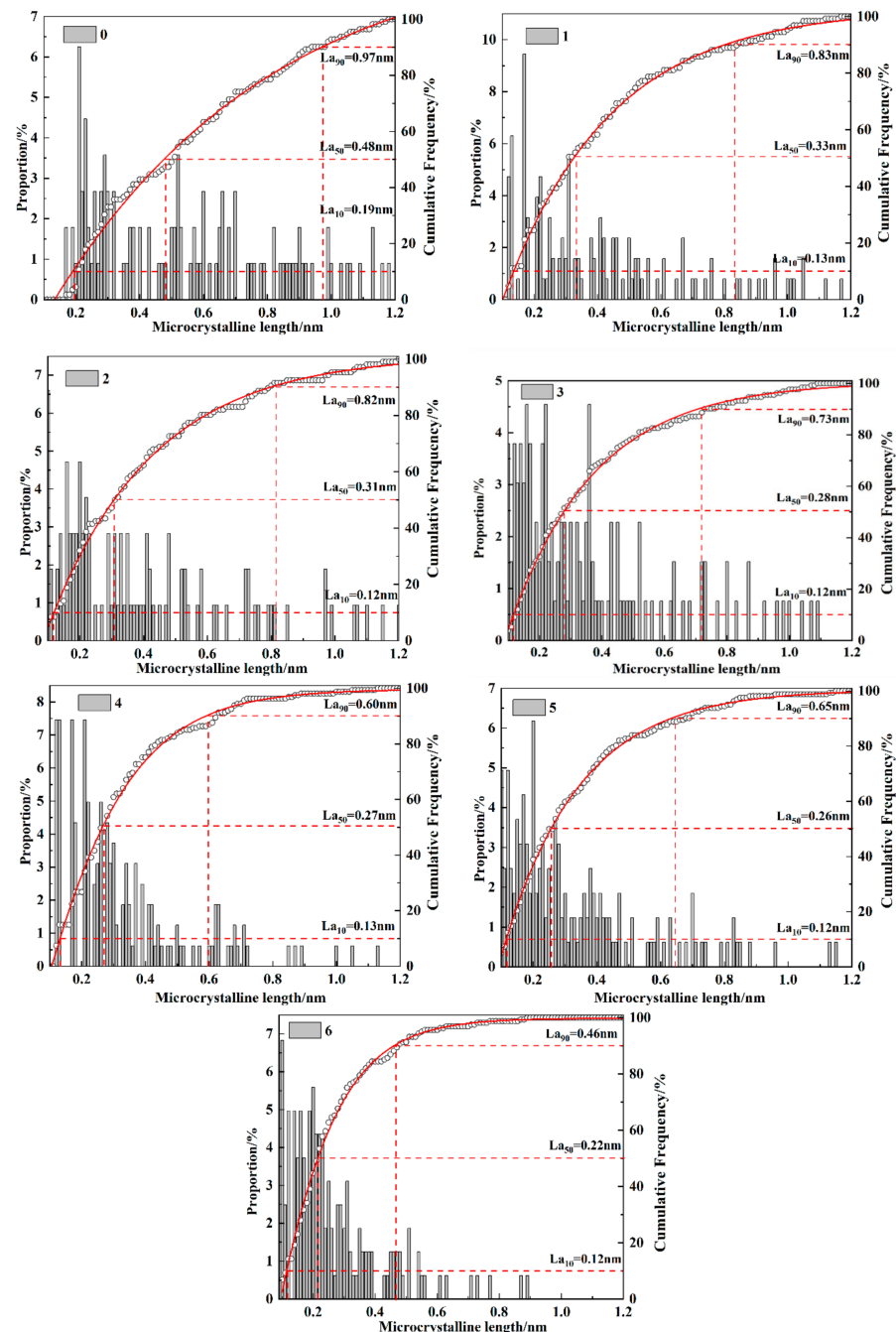


Figure 11. Microcrystalline length distribution of primary carbon particles in carbon black samples.

Figure 12 illustrates the distribution of the dimension spacing (d) of microcrystals in primary carbon particles in the carbon black samples. The dimension spacing of mi-

crocrystals in primary carbon particles in sample 0 before DPF regeneration showed a single-peak distribution, with the peaks concentrated in the range 0.50 nm~0.55 nm, the average dimension spacing was 0.47 nm, and the maximum dimension spacing was not more than 0.60 nm. As the regeneration stage of the DPF advanced, the average dimension spacing of samples 1~4 gradually decreased from 0.46 nm to 0.42 nm. At the same stage, the layer spacing at the regeneration interface was smaller than at the bottom, and the average values of d in samples 5~6 were 0.41 nm and 0.40 nm. After the NTP reaction, the active substances entered into the interior of the primary carbon particles and oxidative reactions occurred, and the long microcrystals in the nucleus were cleaved into fine microcrystals, and the spacing of the cleaved fine microcrystals was shorter and the arrangement of the fine microcrystals was more tight, so the average microcrystalline spacing in the process was decreased dramatically [44].

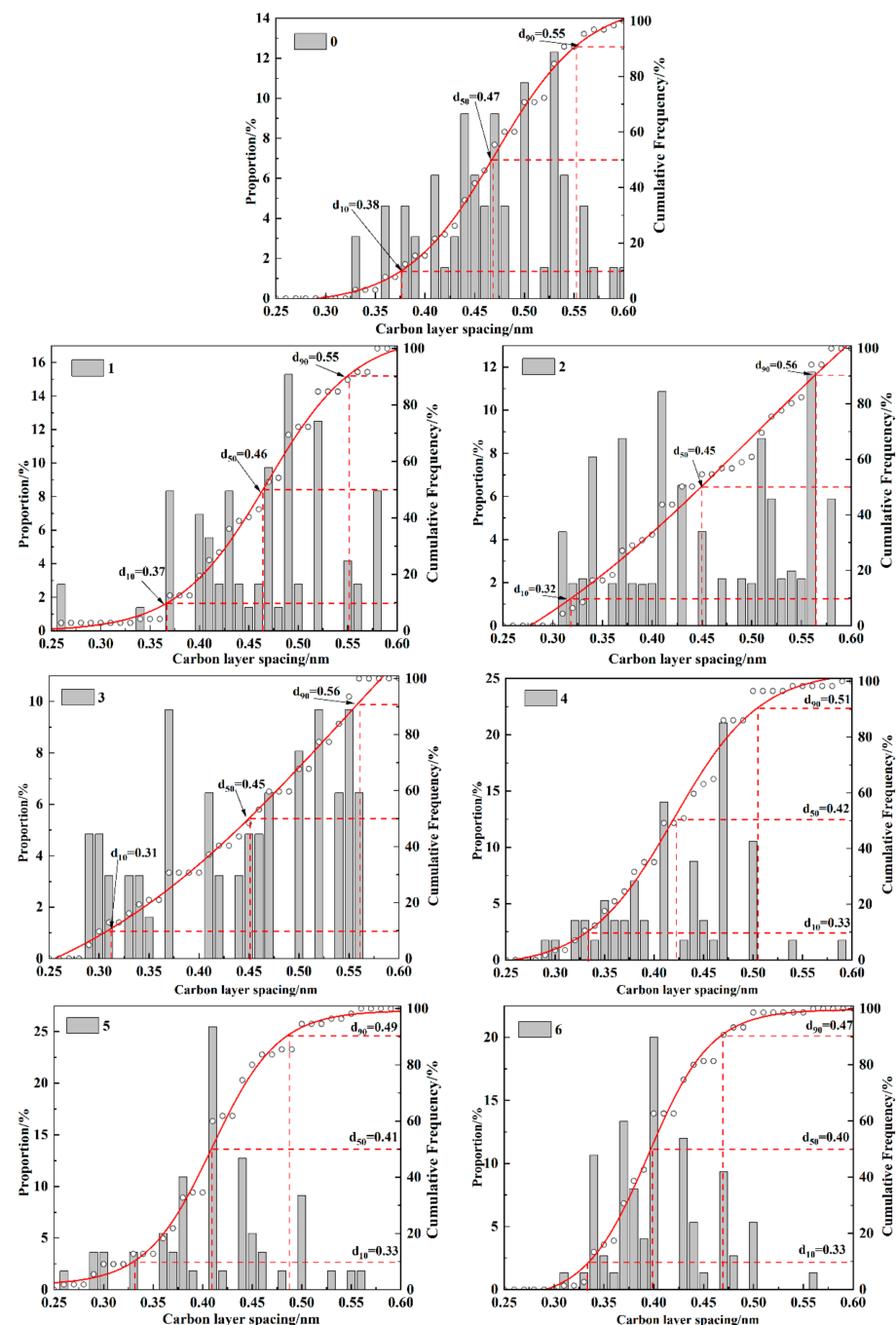


Figure 12. Distribution of primary carbon particle-level spacing in carbon black samples.

Figure 13 illustrates the distribution of microcrystalline curvature (C) of primary carbon particles in the carbon black samples. The average curvature of microcrystals in sample 0 was 1.21. As the DPF regeneration stage advanced, the average microcrystalline curvature of samples 1 to 4 increased from 1.23 to 1.28, and microcrystals with curvatures of 1.50 to 1.60 increased significantly. The microcrystalline curvature at the regeneration interface at the same stage was higher than that at the bottom, and the average values of C in samples 5 and 6 were 1.34 and 1.35, respectively. The higher the microcrystalline curvature of the primary carbon particles, the higher the number of active sites on their surfaces, and the stronger the ability to adsorb reactive oxygen species, so that all the oxidizing activity of carbon black was enhanced [45].

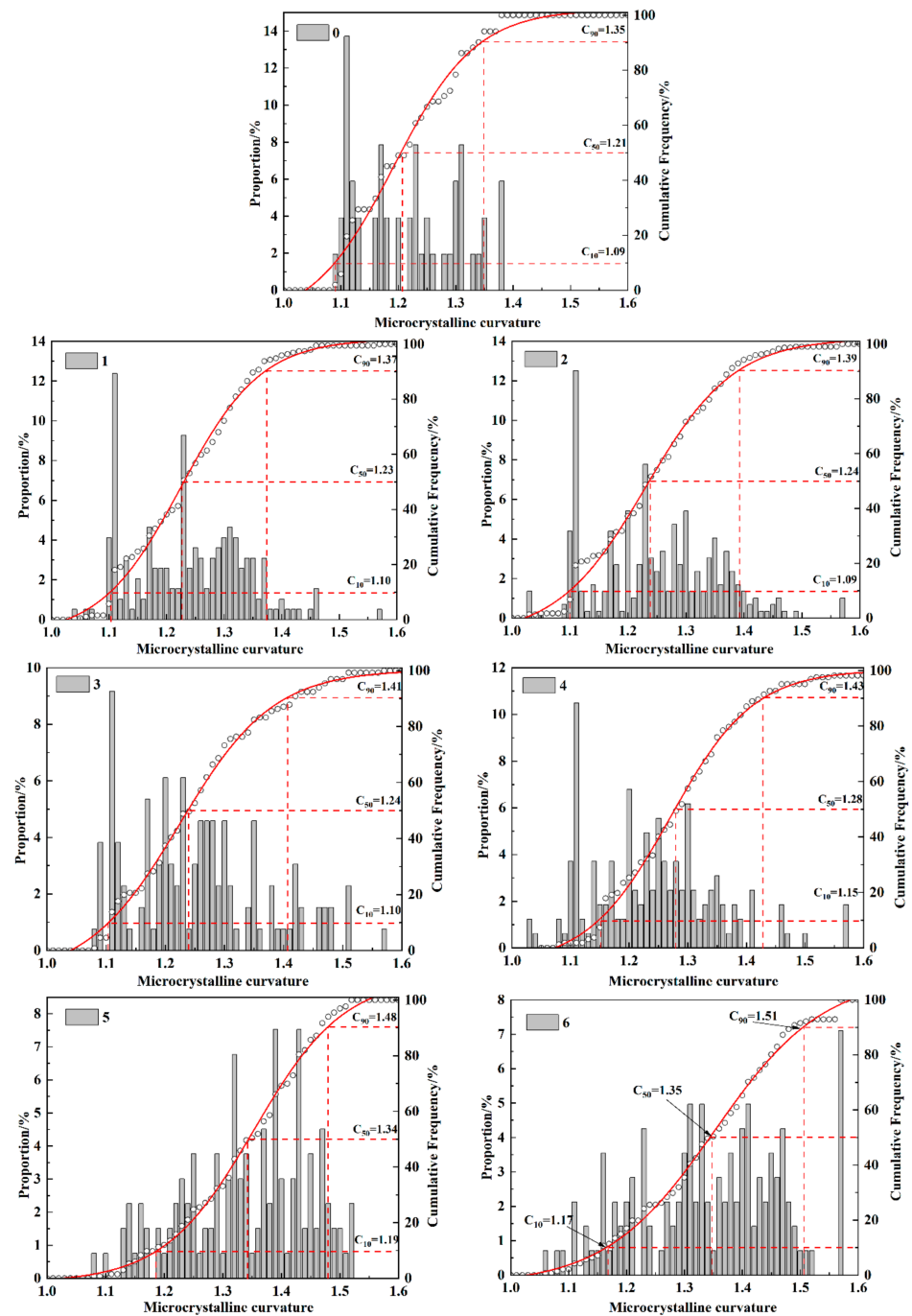


Figure 13. Microcrystalline curvature distribution of primary carbon particles in carbon black samples.

3.4. Degree of Graphitization of Carbon Black Samples

The carbon black samples were placed on glass slides wiped with anhydrous ethanol, and then the samples to be tested were placed on the X-Y automatic platform. Different determination areas of the same sample were selected for repeated determination by microscope to ensure the accuracy of the test sample results.

The Raman test results of carbon black showed strong peaks near 1360 cm^{-1} and 1580 cm^{-1} , which are D peak (Disorder peak) and G peak (Graphite peak), respectively. According to the five-peak fitting method proposed by Sadezky, Table 8 illustrates the Raman peak positions and corresponding structures [46,47]. The first-order Raman spectra of the carbon black samples were fitted to the peaks using Origin2021 software (OriginLab Corp., Northampton, MA, USA), and the fitting results are shown in Figure 14.

Table 8. Raman peak positions and corresponding structures. Reproduced with permission from Xulong Chen, Yunxi Shi et al., Carbon Letters; published by MDPI, 2023 [24].

Location (cm^{-1})	Peak	Corresponding Structures
$\sim 1580\text{ cm}^{-1}$	G	for the E_{2g} symmetric mode, representing the C-C stretching vibration of the sp^2 hybridized atoms located within the carbon layer
$\sim 1360\text{ cm}^{-1}$	D1	A_{1g} mode of symmetry, representing the vibration of structural defects located at the edge of the carbon layer and the impurity elements contained therein
$\sim 1620\text{ cm}^{-1}$	D2	corresponding to the E_{2g} mode of symmetry, representing the vibrations of structural defects located in the graphite layer on the surface of graphite crystals
$\sim 1500\text{ cm}^{-1}$	D3	carbon clusters in the amorphous carbon and functional groups of organic components
$\sim 1180\text{ cm}^{-1}$	D4	corresponding to the A_{1g} mode of symmetry, representing sp^2 – sp^3 hybridization or C-C, C=C stretching vibrations and impurity ions in polyene structures

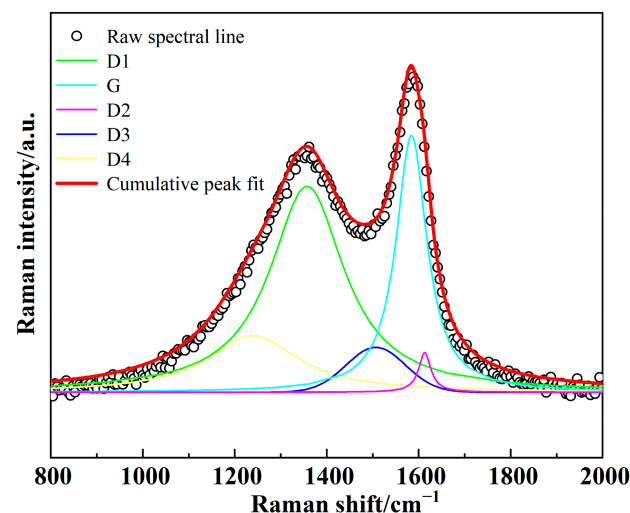


Figure 14. Example of Raman peak fitting for carbon black samples. Reproduced with permission from Xulong Chen, Yunxi Shi et al., Carbon Letters; published by MDPI, 2023 [24].

The relative peak intensity of D1 peak (I_{D1}/I_G) was used to characterize the structural defects at the edge of the graphite microcrystalline carbon layer in the carbon black samples, and the higher the I_{D1}/I_G , the more structural defects in the microcrystals and the higher the disorder. Since I_{D3}/I_G fluctuates greatly, it is difficult to accurately reflect the relative content of amorphous carbon, so the relative peak intensity of the D3 peak, $R_3 = I_{D3}/(I_G + I_{D2} + I_{D3})$, is defined to characterize the content of carbon clusters in the carbon black sample. A high percentage of carbon clusters is usually considered to enhance the oxidizing activity [48]. I_{D1}/I_G and R_3 of the carbon black samples are shown in Figure 15. As seen in Figure 14, I_{D1}/I_G of sample 0 is 4.27, and the most structural defects

were found at the edge of the microcrystalline carbon layer of the carbon black before DPF regeneration. After the NTP reaction, I_{D1}/I_G of carbon black samples 1~4 decreased from 3.31 to 3.10; I_{D1}/I_G of Samples 5~6 located at the regeneration interface were decreased dramatically to 2.98 and 2.54, indicating that the structural defects at the edges of the microcrystalline carbon layer were reduced. The $R3$ values of the carbon black samples were significantly increased after the NTP reaction. $R3$ of samples 1~4 increased from 0.41 to 0.47, and that of samples 5~6 were 0.52 and 0.58, respectively, which indicated that the content of carbon clusters in the amorphous carbon increased. The $R3$ of samples 5~6 were 0.52 and 0.58, respectively, and the content of carbon clusters in amorphous carbon increased. The ordering of graphite structure in PM and the oxidation activity of PM were closely related. The stronger the ordering of graphite structure in the carbon material, the relatively weaker its oxidation activity was. From the TG analysis, the oxidizing activity of carbon black was elevated after NTP action. Although the reduction of structural defects at the edge of the microcrystalline carbon layer made the microcrystalline structure more ordered to some extent, the increase in the content of carbon clusters in the amorphous carbon contributed more to the disorder of the microcrystalline structure, which made the oxidizing activity of the final carbon black enhanced.

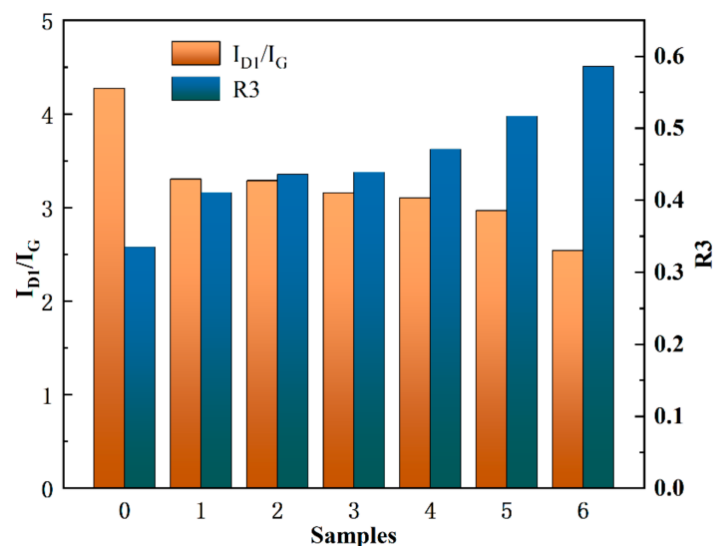


Figure 15. I_{D1}/I_G and $R3$ of carbon black samples.

4. Conclusions

A test system for regeneration of DPFs by NTP oxidation was set up to carry out regeneration tests at different stages on a DPF loaded with carbon black. The carbon black was sampled at the regeneration interface and at the bottom position, and the changes in the physicochemical properties of the carbon black samples during the regeneration of the DPF were analyzed by TG, XPS, HRTEM, and RNS. The main conclusions are as follows:

- (1) As the DPF regeneration stage advanced, the T_s , T_{max} , and T_e of carbon black samples 1~4 decreased. After regeneration, the activation energy of carbon black at the bottom of the DPF gradually decreases. The activation energy of the carbon black sample at the regeneration interface was lower than that at the bottom, and its oxidation activity was stronger.
- (2) With the advancement of the DPF regeneration process, the average microcrystalline length and the average microcrystalline curvature of the primary carbon particles in the carbon black sample increased. The decrease in microcrystalline length and interlayer spacing of carbon particles leads to a denser structure, which leads to an increase in the curvature of carbon particles and an increase in the number of surface active sites. The number of sites increased and the oxidation activity increased.

- (3) The proportion of C element in carbon black before regeneration was 88.4% and O element was 11.6%. After the NTP reaction, the proportion of C element decreased and the proportion of O element increased. The increase in oxygen-containing functional groups in carbon black indicated that the oxidizing activity of carbon black was enhanced, and the increase in amorphous carbon content played a major role in the decrease of graphitization degree of carbon black.
- (4) The DPF was continuously consumed by the reaction with carbon black during the transfer from the top to the bottom, resulting in a gradual decrease in the concentration of NTP active substances from the NTP flow direction. At the same regeneration stage, the highest reaction temperature at the regeneration interface was higher than that at the bottom, so the oxidative decomposition reaction between NTP and carbon black at the regeneration interface was more intense than that at the bottom, and the oxidation process of carbon black was faster.

Author Contributions: Y.L.: Conceptualization, Methodology, Investigation, Visualization; Y.S.: Methodology, Formal analysis, Investigation, Writing—original draft, Project administration; K.Z.: Methodology, Resources; R.J.: Writing—review and editing; X.C.: Writing—original draft, Formal analysis; Y.H.: Formal analysis; Z.W.: Formal analysis; Y.C.: Supervision, Funding acquisition; X.L.: Project administration. All authors have read and agreed to the published version of the manuscript.

Funding: This research was funded by the National Natural Science Foundation of China (No. 52276115), the Major Projects of Natural Science Research in Colleges and Universities in Jiangsu Province (No. 21KJA470001), and Key funded projects of the 2023 Jiangsu Province College Student Innovation and Entrepreneurship Training Program (202310299069Z).

Data Availability Statement: No new data were created or analyzed in this study. Data sharing is not applicable to this article.

Conflicts of Interest: The authors declare no conflicts of interest.

References

- Gao, J.; Chen, H.; Chen, J.; Ma, C.; Tian, G.; Li, Y. Explorations on the continuous oxidation kinetics of diesel PM from heavy-duty vehicles using a single ramp rate method. *Fuel* **2019**, *248*, 254–257. [\[CrossRef\]](#)
- Ruehl, C.; Smith, J.D.; Ma, Y.; Shields, J.E.; Burnitzki, M.; Sobieralski, W.; Ianni, R.; Chernich, D.J.; Chang, M.O.; Collins, J.F.; et al. Emissions During and real-world frequency of heavy-duty diesel particulate filter regeneration. *Environ. Sci. Technol.* **2018**, *52*, 5868–5874. [\[CrossRef\]](#) [\[PubMed\]](#)
- Munoz, X.; Barreiro, E.; Bustamante, V.; Lopez-Campos, J.L.; Gonzalez-Barcala, F.J.; Cruz, M.J. Diesel exhausts particles: Their role in increasing the incidence of asthma. Reviewing the evidence of a causal link. *Sci. Total. Environ.* **2019**, *652*, 1129–1138. [\[CrossRef\]](#) [\[PubMed\]](#)
- Yildiz, I.; Caliskan, H.; Mori, K. Effects of cordierite particulate filters on diesel engine exhaust emissions in terms of pollution prevention approaches for better environmental management. *J. Environ. Manage.* **2021**, *293*, 112873. [\[CrossRef\]](#) [\[PubMed\]](#)
- Wihersaari, H.; Pirjola, L.; Karjalainen, P.; Saukko, E.; Kuuluvainen, H.; Kulmala, K.; Keskinen, J.; Ronkko, T. Particulate emissions of a modern diesel passenger car under laboratory and real-world transient driving conditions. *Environ. Pollut.* **2020**, *265 Pt B*, 114948. [\[CrossRef\]](#)
- Zhong, H.; Tan, J.; Wang, Y.; Tian, J.; Hu, N.; Cheng, J.; Zhang, X. Effects of a Diesel Particulate Filter on Emission Characteristics of a China II Non-road Diesel Engine. *Energy Fuels* **2017**, *31*, 9833–9839. [\[CrossRef\]](#)
- Kuwahara, T.; Nakaguchi, H.; Kuroki, T.; Okubo, M. Continuous reduction of cyclic adsorbed and desorbed NO(x) in diesel emission using nonthermal plasma. *J. Hazard. Mater.* **2016**, *308*, 216–224. [\[CrossRef\]](#)
- Kuwahara, T.; Yoshida, K.; Hanamoto, K.; Sato, K.; Kuroki, T.; Okubo, M. Effect of exhaust gas temperature on oxidation of marine diesel emission particulates with nonthermal-plasma-induced ozone. *Ozone Sci. Eng.* **2015**, *37*, 518–526. [\[CrossRef\]](#)
- Ma, C.; Gao, J.; Zhong, L. Experimental investigation of the oxidation behaviour and thermal kinetics of diesel particulate matter with non-thermal plasma. *Appl. Therm. Eng.* **2016**, *99*, 1110–1118. [\[CrossRef\]](#)
- Liu, L.; Li, X.; Wang, H. Application of combined plasma-catalytic method for carbon particulate matter (pm) removal. *RSC Adv.* **2015**, *5*, 40012–40017. [\[CrossRef\]](#)
- Fushimi, C.; Madokoro, K.; Yao, S. Influence of polarity and rise time of pulse voltage waveforms on diesel particulate matter removal using an uneven dielectric barrier discharge reactor. *Plasma Chem. Plasma Process.* **2008**, *28*, 511–522. [\[CrossRef\]](#)
- Hongsuk, K.; Hoyeol, L.; Sunyoup, L. Combustion efficiency of a plasma-ignited diesel burner for dpf regeneration. *SAE Technical. Papers* **2023**, *21*, 04–14.

13. Shi, Y.; Cai, Y.; Li, X.; Pu, X.; Zhao, N.; Wang, W. Effect of the amount of trapped particulate matter on diesel particulate filter regeneration performance using non-thermal plasma assisted by exhaust waste heat. *Plasma Sci. Technol.* **2020**, *22*, 91–99. [\[CrossRef\]](#)
14. Shi, Y.; Cai, Y.; Li, X.; Chen, Y.; Ding, D.; Tang, W. Mechanism and method of DPF regeneration by oxygen radical generated by NTP technology. *Int. J. Automot. Eng.* **2014**, *15*, 871–876. [\[CrossRef\]](#)
15. Shi, Y.; Cai, Y.; Li, X.; Xu, H.; Li, W.; Pu, X. Low temperature diesel particulate filter regeneration by atmospheric air non-thermal plasma injection system. *Plasma Chem. Plasma Process.* **2016**, *36*, 783–797. [\[CrossRef\]](#)
16. Zouaoui, N.; Brillhac, J.F.; Mechat, F.; Jeguirim, M.; Djellouli, B.; Gilot, P. Study of experimental and theoretical procedures when using thermogravimetric analysis to determine kinetic parameters of carbon black oxidation. *J. Therm. Anal. Calorim.* **2010**, *102*, 837–849. [\[CrossRef\]](#)
17. Choi, G.B.; Kim, Y.-A.; Hong, D.; Choi, Y.; Yeon, S.-H.; Park, Y.-K.; Lee, G.-G.; Lee, H.; Jung, S.-C. Carbon black produced by plasma in benzene solution applied as the conductive agent in lithium secondary batteries. *Carbon* **2023**, *205*, 444–453. [\[CrossRef\]](#)
18. Ranji-Burachaloo, H.; Masoomi-Godarzi, S.; Khodadadi, A.A.; Mortazavi, Y. Synergetic effects of plasma and metal oxide catalysts on diesel soot oxidation. *Appl. Catal. B* **2016**, *182*, 74–84. [\[CrossRef\]](#)
19. Naseri, A.; Sediako, A.D.; Liu, F.; Barati, M.; Baker, R.D.; Thomson, M.J. In-situ studies of O₂ and O radical oxidation of carbon black using thermogravimetric analysis and environmental transmission electron microscopy. *Carbon* **2020**, *156*, 299–308. [\[CrossRef\]](#)
20. Tighe, C.J.; Twigg, M.V.; Hayhurst, A.N.; Dennis, J.S. The kinetics of oxidation of Diesel soots and a carbon black (Printex U) by O₂ with reference to changes in both size and internal structure of the spherules during burnout. *Carbon* **2016**, *107*, 20–35. [\[CrossRef\]](#)
21. Meng, Z.; Zeng, B.; Tan, J.; Chen, Z.; Ou, J. Study of gas and particulate emission characteristics during the fast regeneration period of DPF. *Fuel* **2022**, *317*, 123353. [\[CrossRef\]](#)
22. Meng, Z.; Yang, D.; Yan, Y. Study of carbon black oxidation behavior under different heating rates. *J. Therm. Anal. Calorim.* **2014**, *118*, 551–559. [\[CrossRef\]](#)
23. Fang, J.; Meng, Z.; Li, J.; Pu, Y.; Du, Y.; Li, J.; Jin, Z.; Chen, C.; Chase, G.G. The influence of ash on soot deposition and regeneration processes in diesel particulate filter. *Appl. Therm. Eng.* **2017**, *124*, 633–640. [\[CrossRef\]](#)
24. Chen, X.; Shi, Y.; Cai, Y.; Xie, J.; Yang, Y.; Hou, D.; Fan, Y. Effect of non-thermal plasma injection flow rate on diesel particulate filter regeneration at room temperature. *Carbon Lett.* **2024**, *33*, 97–101. [\[CrossRef\]](#)
25. Shi, Y.; Lu, Y.; Cai, Y.; He, Y.; Zhou, Y.; Fang, J. Evolution of particulate matter deposited in the DPF channel during low-temperature regeneration by non-thermal plasma. *Fuel* **2022**, *318*, 123552. [\[CrossRef\]](#)
26. Cavallo, D.M.; Chiavola, O.; Palmieri, F.; Mancaruso, E.; Vaglieco, B.M. Experimental study on the effect of loading and regeneration for an optimized management of the DPF. *Results Eng.* **2023**, *18*, 101048. [\[CrossRef\]](#)
27. Biesinger, M.C. Assessing the robustness of adventitious carbon for charge referencing (correction) purposes in XPS analysis: Insights from a multi-user facility data review. *Appl. Surf. Sci.* **2022**, *597*, 153681. [\[CrossRef\]](#)
28. Wang, L.; Xuan, C.; Zhang, X.; Sun, R.; Cheng, X.; Wang, Z.; Ma, C. NO_x adsorption mechanism of coal-based activated carbon modified with trace potassium: In situ drifts and dft study. *Energy Fuels* **2022**, *36*, 7633–7650. [\[CrossRef\]](#)
29. Yao, S.; Wu, Z.; Han, J.; Tang, X.; Jiang, B.; Lu, H.; Yamamoto, S.; Kodama, S. Study of ozone generation in an atmospheric dielectric barrier discharge reactor. *J. Electrostat.* **2015**, *75*, 35–42. [\[CrossRef\]](#)
30. Gao, J.; Ma, C.; Xing, S.; Sun, L. Oxidation behaviours of particulate matter emitted by a diesel engine equipped with a NTP device. *Appl. Therm. Eng.* **2017**, *119*, 593–602. [\[CrossRef\]](#)
31. Chen, X.; Wang, X.; Fang, D. A review on C1s XPS-spectra for some kinds of carbon materials. *Fuller. Nanotub. Carbon Nanostructures* **2020**, *28*, 1048–1058. [\[CrossRef\]](#)
32. Pu, X.; Cai, Y.; Shi, Y.; Wang, J.; Gu, L.; Tian, J.; Li, W. Diesel particulate filter (DPF) regeneration using non-thermal plasma induced by dielectric barrier discharge. *J. Energy Inst.* **2018**, *91*, 655–667. [\[CrossRef\]](#)
33. Cabiell, M.; Rouzaud, J.; Garcia, A.B. High-resolution transmission electron microscopy studies of graphite materials prepared by high-temperature treatment of unburned carbon concentrates from combustion fly ashes. *Energy Fuels* **2009**, *23*, 942–950. [\[CrossRef\]](#)
34. E, J.; Luo, B.; Han, D.; Chen, J.; Liao, G.; Zhang, F.; Ding, J. A comprehensive review on performance improvement of micro energy mechanical system: Heat transfer, micro combustion and energy conversion. *Energy* **2022**, *239*, 122509. [\[CrossRef\]](#)
35. Gao, J.; Tian, G.; Ma, C.; Chen, J.; Huang, L. Physicochemical property changes during oxidation process for diesel PM sampled at different tailpipe positions. *Fuel* **2018**, *219*, 62–68. [\[CrossRef\]](#)
36. Gao, J.; Ma, C.; Xing, S.; Sun, L.; Huang, L. Nanostructure analysis of particulate matter emitted from a diesel engine equipped with a NTP reactor. *Fuel* **2017**, *192*, 35–44. [\[CrossRef\]](#)
37. Chen, Y.; Chen, Z.; Li, K.; Shi, T.; Chen, X.; Lei, J.; Wu, T.; Li, Y.; Liu, Q.; Shi, B.; et al. Research of carbon emission prediction: An oscillatory particle swarm optimization for long short-term memory. *Processes* **2023**, *11*, 3011. [\[CrossRef\]](#)
38. Chu, H.; Qi, J.; Feng, S.; Dong, W.; Hong, R.; Qiu, B.; Han, W. Soot formation in high-pressure combustion: Status and challenges. *Fuel* **2023**, *345*, 128236. [\[CrossRef\]](#)
39. Gao, J.; Ma, C.; Xia, F.; Xing, S.; Sun, L.; Huang, L. Raman characteristics of PM emitted by a diesel engine equipped with a NTP reactor. *Fuel* **2016**, *185*, 289–297. [\[CrossRef\]](#)

40. Mo, W.L.; Ren, Y.; Ma, Y.; Guo, J.; Feng, Z.H.; Zhang, S.P.; Yang, X.Q. Structure characteristics and removal behavior of the deposited carbon on ni-Al₂O₃ catalyst for CO₂ reforming of CH₄. *Processes* **2023**, *11*, 2968. [[CrossRef](#)]
41. Chen, G.; Wei, F.; Zhang, K.; Xiao, R.; Wang, Z.; Yang, S. Investigation on combustion characteristics and gas emissions of a high-pressure direct-injection natural gas engine at different combustion modes. *Energy Convers. Manag.* **2023**, *277*, 116617. [[CrossRef](#)]
42. Salamanca, M.; Mondragón, F.; Agudelo, J.R.; Santamaría, A. Influence of palm oil biodiesel on the chemical and morphological characteristics of particulate matter emitted by a diesel engine. *Atmos. Environ.* **2012**, *62*, 220–227. [[CrossRef](#)]
43. Shi, Y.; Yang, Y.; He, Y.; Cai, Y.; Xie, J.; Chen, X.; Ding, Z. Effect of reaction temperature on the degradation and oxidation behavior of particulate matter by nonthermal plasma. *Fuel* **2024**, *359*, 130312. [[CrossRef](#)]
44. Chu, H.; Feng, S.; Hong, R.; Ma, X.; Qiao, F.; Chen, L. Effects of ammonia addition on soot formation in hydrocarbon fuels combustion: Challenges and prospects. *Fuel* **2024**, *360*, 130569. [[CrossRef](#)]
45. Zhang, K.; Liu, H.; Ma, M.; Xu, H.; Fang, H. Multiscale fractal characterization of pore–fracture structure of tectonically deformed coal compared to primary undeformed coal: Implications for CO₂ geological sequestration in coal seams. *Processes* **2023**, *11*, 2934. [[CrossRef](#)]
46. Sadezky, A.; Muckenhuber, H.; Grothe, H.; Niessner, R.; Pöschl, U. Raman microspectroscopy of soot and related carbonaceous materials: Spectral analysis and structural information. *Carbon* **2005**, *43*, 1731–1742. [[CrossRef](#)]
47. Wang, Y.; Liang, X.; Tang, G.; Chen, Y.; Dong, L.; Shu, G. Impact of lubricating oil combustion on nanostructure, composition and graphitization of diesel particles. *Fuel* **2017**, *190*, 237–244. [[CrossRef](#)]
48. Natalia, P.; Ivleva, A.; Xin, Y. Raman microspectroscopic analysis of changes in the chemical structure and reactivity of soot in a diesel exhaust aftertreatment model system. *Environ. Sci. Technol.* **2007**, *41*, 3702–3707.

Disclaimer/Publisher’s Note: The statements, opinions and data contained in all publications are solely those of the individual author(s) and contributor(s) and not of MDPI and/or the editor(s). MDPI and/or the editor(s) disclaim responsibility for any injury to people or property resulting from any ideas, methods, instructions or products referred to in the content.